Additive Manufacturing 59 (2022) 103123

Contents lists available at ScienceDirect

Additive Manufacturing

journal homepage: www.elsevier.com/locate/addma

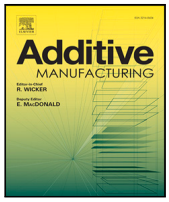

Research paper

Material extrusion additive manufacturing and experimental testing of topology-optimised passive heat sinks using a thermally-conductive plastic filament

Eetu Huttunen [a], Mikko T. Nykänen [a], Joe Alexandersen [b,*]

[a] Electronics 3K Factory, South-Eastern Finland University of Applied Sciences (XAMK), Laitaatsillantie 3, 57170 Savonlinna, Finland
[b] Department of Mechanical and Electrical Engineering, University of Southern Denmark, 5230 Odense, Denmark

ARTICLE INFO

Keywords:
Material extrusion
Topology optimisation
Thermal conduction
Heat sink

ABSTRACT

This paper presents an experimental study of topology-optimised passive heat sinks produced in a thermally-conductive plastic using material extrusion additive manufacturing. The thermal performance of the filament is investigated through test printing, thermal conductivity testing and scanning electron microscope imaging. Topology optimisation is used to generate novel heat sink designs for passive cooling through natural convection. The optimised designs are complex and are printed using soluble support materials. The measured anisotropic thermal conductivity of the layer-by-layer additively manufactured specimens is included in the topology optimisation process to design heat sinks specifically with the chosen filament and process in mind. It is shown that when taking the material anisotropy into account, the topology-optimised heat sinks deliver up to 10–20% reduction in thermal resistance compared to a reference straight-fin design.

1. Introduction

Applications for electronics cooling have evolved recently, such as various battery-powered devices, aerospace applications and portable/wearable mobile devices. In these applications, low weight, ease-of-use, corrosion and chemical resistance have emerged as new requirements for cooling solutions. Various plastic-based solutions that are lightweight, corrosion and chemical resistant have begun to be developed for such applications. Another requirement is a lack of electrical conductivity. Heat sinks are designed to transfer heat away from a heat source to another medium, usually a surrounding fluid flow. However, their shapes can often cause significant electromagnetic interference [1,2]. This can be a huge problem in aerospace and telecommunication applications. Furthermore, in aerospace applications, metal heat sinks increase the risk of short circuits and, thus, fires, requiring electrical grounding. Therefore, plastic-based solutions with a low electrical conductivity, but relatively high thermal conductivity, are relevant to investigate for heat sink applications. Lastly, ecological aspects of the manufacturing process has contributed to research into alternative materials suitable for cooling applications. Additive manufacturing as a manufacturing method has many additional design freedoms compared to traditional methods, allowing for more complex structures of heat sinks. For this reason, additive manufacturing is often used to produce complex structures that are optimised for efficient cooling [3,4]. However, there are also challenges in using additive manufacturing methods. This study examines in detail how a plastic filament is suitable for heat sinks and how structures generated using topology optimisation can be fabricated in practice using additive manufacturing.

1.1. Concepts and literature

1.1.1. Additive manufacturing

In recent years, there has been a growing interest in using additive manufacturing in connection with various functional applications. In particular, the achievement of complex structures through additive manufacturing have encouraged the development and deployment of a variety of functional materials. Additive manufacturing is a step towards the next generation and revolution in the manufacturing industry. Functional materials can be found in applications such as electronics, sensors, robotics and medical devices. For cooling solutions, the latest developments in the use of thermally-conductive plastic materials using additive manufacturing was recently reviewed by Zhang et al. [5].

Electronics cooling is an active area of research, and its improvement and development to become more environmentally friendly has

* Corresponding author.
E-mail address: joal@sdu.dk (J. Alexandersen).

https://doi.org/10.1016/j.addma.2022.103123
Received 20 April 2022; Received in revised form 8 August 2022; Accepted 31 August 2022
Available online 6 September 2022

sparked the development of thermally-conductive plastics. As previously mentioned, corrosion resistance and low electrical conductivity is also highly relevant. Additive manufacturing methods have recently been able to produce a variety of complex structures suitable for cooling [3,4]. Simulation-based design optimisation, such as the topology optimisation method [6], often generates complex organic shapes that are highly performant. In order to manufacture these structures, thermally-conductive extrudable plastics have been developed for various cooling solutions. The thermal conductivity of these plastics has been improved by various additives, such as graphite, metals and so on [5,7,8]. Jing et al. [9] combined solid-state shear milling (S3M) and material extrusion technology to improve thermal conductivity of linear low-density polyethylene (LLDPE). Graphene nanoplatelets were used as filler to enhance thermal conductivity of the LLDPE plastic. The fabricated parts exhibited a significantly enhanced cross-layer thermal conductivity up to 3.43 W/(m K) compared to 0.40 W/(m K) for pure LLDPE. Guo et al. [10] fabricated graphene and thermoplastic polyurethane (TPU) composite filaments. Sample pieces were printed using material extrusion technology. Cross-layer thermal conductivity of 12 W/(m K) was achieved. Timbs et al. [11] investigated performance of straight and oblique fin heat sink made of thermally-conductive plastic composites. The heat sinks were additively-manufactured using Ice9 Flex (carbon filled plastic), copper filled filament (polylactic acid with copper particles) and bronze filled filament (polylactic acid with bronze particles). The carbon-filled plastic heat sink was shown to have much superior heat dissipation capability compared to metal-filled filament heat sinks.

1.1.2. Topology optimisation

Topology optimisation is a simulation-based design optimisation method, which harnesses an ultimate design freedom of being able to generate a novel concept without an a priori design [6]. The user defines the physical problem, boundary conditions, and the design domain within which the design is allowed to be generated. Topology optimisation formulates the design problem as a material distribution problem, which in the context of conjugate heat transfer becomes: where to place solid material forming conductive members and where to place fluid passages to transfer heat away from the solid.

Topology optimisation usually generates complex and organic designs, which are not readily producible using traditional manufacturing methods. Additive manufacturing has become an obvious ally of topology optimisation given the large degree of geometric complexity allowed by the layer-by-layer process, as well as the significant development and democratisation over the past decade. However, the additive manufacturing process still has its limitations, which should ideally be taken into account in the simulations of additively-manufactured geometries. The recent review paper on topology optimisation for additive manufacturing by Liu et al. [12] discusses the large array of work on the subject so far.

Due to the layer-by-layer process, inherently there will be anisotropy present in the material properties. Two main directions can be identified as the in-layer (or in-plane) and the cross-layer (or through-plane), where the first is in directions within each layer and the second is in the direction perpendicular to the layers. The effective properties of a manufactured design will be close to the base material in the in-layer direction, at least in the directions of the deposition sequence. In contrast, it will be significantly lower in the cross-layer direction due to non-perfect bonding between the layers. For heat conduction problems, this results in a lowered thermal conductivity in the cross-layer direction as will be shown in Section 3.2. The importance of the anisotropic properties on topology optimisation of load bearing structures is discussed by Zhang et al. [13]. Previous work on including the inherent material anisotropy in the topology optimisation process is relatively limited, e.g.: Mirzendehdel et al. [14] incorporate an orthotropic material strength model to accurately capture layer adhesion failures due to reduced cross-layer properties; Dapogny et al. [15] instead consider the orthotropic nature of the elastic properties within discrete layers, where a lower Young's modulus is introduced in the normal direction to the print lines; Zhang et al. [16] present topology optimisation for heat conduction with anisotropic thermal conductivity. It is also possible to explicitly optimise the local material anisotropy for various purposes, such as continuous fiber reinforcement [17] and heat flux manipulation [18].

Topology optimisation of fluid flow and conjugate heat transfer is now a mature, yet rapidly developing, field of research. A recent review paper [19] showed that since 2010, 55 papers on the subject had been published up to February 2020. Of these papers, only 7 considered manufacture and experimental testing of the numerically-optimised heat sinks: forced convection heat sinks using milling [20–22]; forced convection heat sinks using metal additive manufacture [23,24]; natural convection heat sinks using metal additive manufacture [25]; natural convection heat sinks using additive manufacturing assisted investment casting [26]. Since the review paper was published, more publications treating manufacture and experimental testing have been published all treating forced convection heat sinks: milling [27–29]; metal additive manufacture [30]; milling, porous foams and cylindrical pins [31].

1.1.3. Passive cooling heat sinks

Natural convection is the phenomena of fluid flow happening not due to external pressure or velocity sources (fans, pumps, suction, etc.), but rather due to density variations of the fluid itself. Passive cooling is the concept of exploiting natural convection for cooling purposes. Here the density variations arise due to the heating of the fluid by a heat source, causing the density to decrease and the fluid to rise due to buoyancy differences compared to the surrounding cooler fluid. Thus, for electronics cooling, this provides a "free" sources of cooling, since the heat sources are generating waste heat, which causes hot air to rise and drawing in cool air from the surrounding to replace it, thereby cooling the heat source. This is the main benefit of passive cooling, it exploits the naturally occurring air currents and cools without the need for a fan or pump, making it entirely noiseless. However, the main drawback is a limitation to the obtainable convection heat transfer coefficient, which is low compared to forced convection [32].

Design of heat sinks for passive cooling is quite different than for forced convection. Natural convection has a two-way coupling between the fluid flow and heat transfer, where not only does the fluid flow drive the convective heat transfer, but the arising temperature field drives the fluid flow. This means that when maximising the natural convection heat transfer, it inherently requires the flow resistance to be low to allow the fluid to flow easily through it. For straight fin heat sinks, this manifests itself in a natural lower bound on the spacing between the fins [33]: too small spacing (and too many fins) and the fluid cannot flow, too large spacing (and too few fins) and the heat transfer surface area will be too low. For passive cooling of light-emitting diode (LED) lamps, this has been observed in practice using topology optimisation [25,34], where open and non-dense topology-optimised heat sinks are seen to perform significantly better than dense lattice designs. The work highlights that the common idea of "more surface area = better heat transfer" is not always true, especially for natural convection. The fact that topology-optimised heat sinks have significantly lower surface area, but better cooling, shows that it is more about where to place and how to shape the convection surface.

1.2. Contributions

This study investigates the printing properties and performance of a thermally-conductive plastic developed for additive manufacturing using the material extrusion method called Fused Filament Fabrication (FFF) method. Fused Filament Fabrication is most common and widely known AM technique. In this technique, a solid thermoplastic filament form material is extruded through a nozzle heated to the melting point

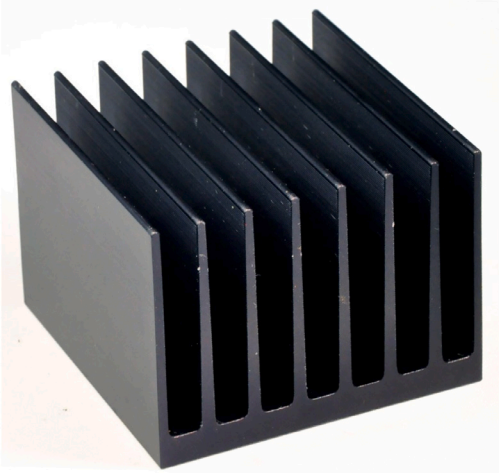

Fig. 1. The reference straight-fin heat sink made of extruded aluminium. Photography by Mari Rasku.

of the material. The printed piece is formed layer by layer according to the 3D model using the movements of the print head and the build plate [35]. The study has been performed through experimental tests and scanning electron microscope (SEM) imaging. Several heat sinks were printed from the material and compared to a correspondingly sized reference straight-fin heat sink in both the filament and extruded aluminium. The study restricts itself to passive cooling through natural convection, with radiant heat transfer contributions. The design freedoms of topology optimisation and additive manufacturing is fully exploited in the design and manufacture of heat sinks. Heat sink design solutions for a thermally-conductive plastic material were generated using topology optimisation taking the measured anisotropic thermal conductivity into account based on the build direction. Designs were also generated assuming an isotropic thermal conductivity, with the value from both provided data sheets and measured values. The optimised designs are all compared to the reference straight-fin heat sink in both the conductive filament and extruded aluminium. It is seen that topology-optimised heat sink designs perform better than the reference design and that taking the material anisotropy into account during topology optimisation provides a measurable difference in performance.

2. Design problem

2.1. Reference heat sink

As a starting point for the study, a straight-fin heat sink commonly used in cooling applications is chosen as the reference design. The size of the heat sink and thickness of fins is selected based on the minimum geometric detail level possible to reliably manufacture using the material extrusion process described in Section 3.3. By printing experiments, the smallest reasonable feature detail that could reliably be produced with high quality was around 2–3 mm. Therefore, there is no guarantee that it is the best possible reference design.

The Aavid Thermalloy 637303B03000 heat sink manufactured of extruded aluminium is selected and is shown in Fig. 1. The outer dimensions of the heat sink are 76.1 mm × 76.1 mm × 57.15 mm. The fin width is 3 mm and 2 mm at the base and tip, respectively, and the fin spacing is 7 mm at the base. The heat sink has a 7 mm thick base plate to which the fins are joined. The thermal resistance is 1.88 °C/W according to the manufacturer [36].

2.2. Design domain

The design domain of the topology-optimised heat sinks is based on the same outer dimensions and base plate thickness as the reference heat sink. The input data for the design of topology-optimised heat sinks is shown in Fig. 2. The design space (yellow) is 76 mm × 76 mm × 50 mm and the fixed non-design region (green) is 76 mm × 76 mm × 7 mm. The heat source is attached to the bottom surface of the heat sink in an area of 56 mm × 56 mm (grey). The power of the heat source set to 15 W and is assumed to be uniformly distributed. The design was done in two different directions of gravity: direction G1 corresponds to a vertical wall installation; and G2 corresponds to a horizontal wall installation.

3. Additive manufacturing process

3.1. Filament information

The material used in this study is called Ice9 Rigid Nylon and is manufactured by TCpoly. The material is available in filament form in diameters of 1.75 mm and 2.85 mm. The material is intended to be used in material extrusion additive manufacturing. According to the composition stated by the manufacturer, the base plastic of the material is PA12. The manufacturer does not provide more detailed information on the composition of the material, such as ingredients that provide better thermal conductivity compared to pure polyamide plastic [37].

The manufacturer declares the thermal conductivity of the material to be 4 W/(m K) in-layer and 1 W/(m K) cross-layer [38]. For comparison, the thermal conductivity of the pure PA12 plastic used as the base plastic of the material is about 0.3 W/(m K) [39]. The thermal conductivity in the manufactured part is lower in the direction across the layers than in directions within the layer. This affects the build direction in which the heat sink is additively manufactured, such that the heat is transferred away from the heat source as efficiently as possible. It is ideal to orient the layers in directions that are perpendicular to the heat source, rather than parallel to it.

Differences in the thermal conductivity of the printed parts are due to the structure and properties of the material extrusion technology during the printing process. The filament is fed to the nozzle which is heated to the melting point of the material. By the movement of the nozzle or the printer bed, the molten material is extruded to form a geometry as it cools. The method produces one layer at a time proceeding in the height direction. A single layer consists of lines printed side by side. Ideally, both adjacent print lines within the same layer and in adjacent layers merge completely together. Ideally, the cross-section of the print line is rectangular. However, in practice the corners of the rectangle are rounded due to the properties of the material coming from the nozzle. This causes small air gaps in the structure between the layers and the print lines, which can clearly be seen in Fig. 3. However, air gaps formed during the print process can be affected by the print settings. By changing the print settings, the size of air gaps in the part can be minimised which in turn has a positive effect on the final cooling properties of the part.

3.2. Thermal conductivity testing

The study examines the thermal conductivity of Ice9 Rigid Nylon material for two different printing directions. A thermal conductivity testing apparatus meeting the ASTM C1044-98 standard [40] is prepared. The thermal conductivity testing uses the one-sided guarded hot plate method with a single sample. The method is suitable for materials with poor to low thermal conductivity. Therefore, the guarded hot plate method was chosen together with a reasonably simple implementation as shown in Fig. 4.

For testing, specimens of dimensions 70 mm × 70 mm × 14 mm and 70 mm × 70 mm × 22 mm were additively-manufactured using the

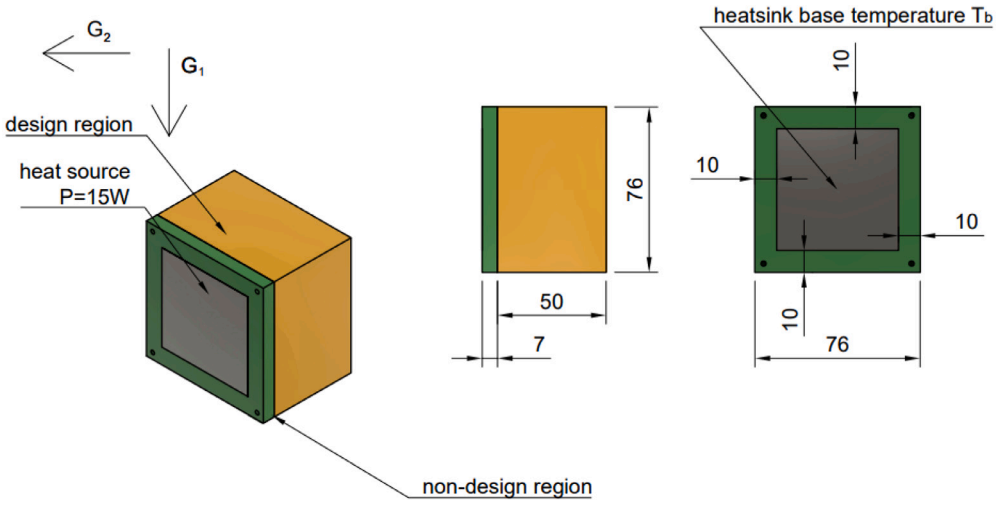

Fig. 2. Design parameters for topology-optimised heat sinks. The non-design region is the base plate of same size as for the reference heat sink and the design region is the same size as the external dimensions of the reference heat sink fins. (For interpretation of the references to colour in this figure legend, the reader is referred to the web version of this article.)

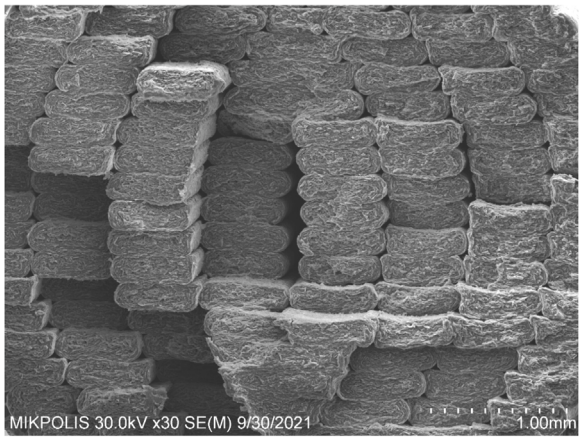

Fig. 3. Internal layer structure of additively-manufactured part made of Ice9 Rigid Nylon material. Image is captured by scanning electron microscope (SEM) of a fracture surface of a test specimen. The printing line width is 0.6 mm and layer height is 0.25 mm. Image by Mikpolis.

Ice9 Rigid Nylon material. As a reference, a polycarbonate sample of dimensions 70 mm × 70 mm × 6 mm was prepared to ensure the functionality and reproducibility of the test setup. Four samples of Ice9 Rigid Nylon were prepared in the two different thicknesses and in two different printing directions to compare the effect of printing direction on thermal conductivity. The thermal conductivity is calculated using:

$$k_{meas} = \frac{t\,Q}{A\left(T_h - T_c\right)} \tag{1}$$

where k_{meas} is the measured thermal conductivity of the sample, t is thickness of the sample, Q is heat flux through the specimen, A is the metered section area of the hot plate added by half of the area of air gap between hot plate and guarded hot plate according to ASTM C177-97 [41], T_h is temperature of the hot plate and T_c is temperature of the cold plate. Table 1 shows the thermal conductivity calculated from the measurements, as well as the value reported by the manufacturer and found in the literature for the reference sample. Results for Ice9 Rigid Nylon material are calculated as average values of the calculated thermal conductivity for the two test specimen thicknesses.

Table 1
Thermal conductivities of the test specimens with limit of error and thermal conductivity reported in the literature [38,39].

Material	Measured k [W/(m K)]	Reported k [W/(m K)]
Ice9 rigid nylon (in-layer)	3.23 ± 0.23	4
Ice9 rigid nylon (cross-layer)	0.88 ± 0.04	1
Polycarbonate reference	0.24 ± 0.02	0.2

3.3. Printing parameters

The manufacture of the heat sinks was performed using a Minifactory Ultra 3D printer. The Minifactory Ultra used the FFF printing technology, meaning that the material is in filament form. The advantage of this device is the possibility of using high temperatures for the nozzles, printing bed and for the printing chamber. The machine has two print nozzles that can be heated to temperatures up to 470 °C. The temperature of the heated glass build plate and the printing chamber can be adjusted in a controlled manner up to 250 °C. A controlled printing environment enables better and more consistent quality for the printed parts [42]. Elevated temperatures allow the use of a very wide range of materials including high-end plastics such as the PEEK, PEKK and PEI plastic families [43]. As mentioned previously, the adhesion between the printing layers affects the heat transfer properties in addition to the mechanical strength. The controlled printing environment offers good adhesion between the printing layers, as well as largely preventing warping effects. Warping refers to the phenomenon in which the specimen tends to pull itself off the printing bed during printing, as the lower layers cool when progressing to the upper layers. As a result of the cooling, the piece shrinks and tends to detach from the printer bed. Lastly, the Minifactory Ultra also has a separate drying chamber for the print material, which ensures that the print material is dry before and during printing. This feature is useful when printing nylon-based materials that are generally sensitive to ambient moisture [42].

The determination of print settings is crucial for the success of the process. For thermally-conductive plastics, the print settings can affect the thermal conductivity of the final specimen. It is important to try to minimise air gaps in the part during printing. In practice, this means adjusting the settings so that the air gaps inside the part are minimised by the amount of material fed (flow), the width of the print lines (line width) and the settings for filling and infill overlap. By adjusting these

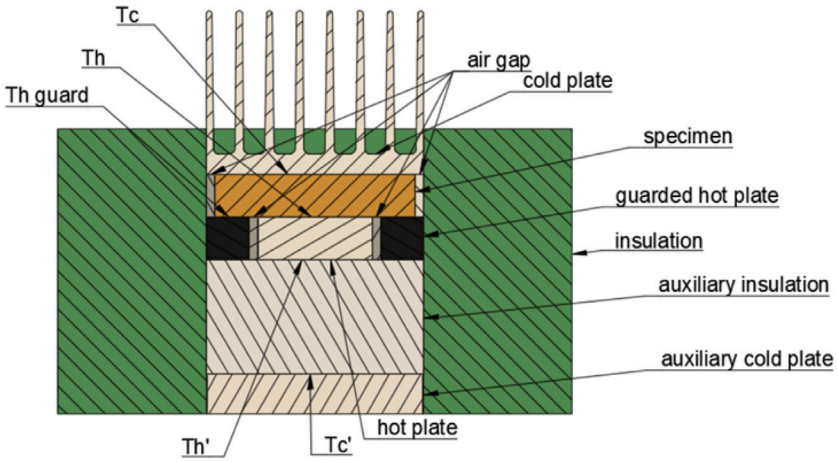

Fig. 4. Cross-section of thermal conductivity testing apparatus. The test specimen is 70 mm × 70 mm with variable thickness.

Table 2
Final printing parameter values determined by printing of test pieces.

Parameter	Value
Nozzle diameter	0.5 mm
Nozzle temperature	295 °C
Bed temperature	60 °C
Chamber temperature	60 °C
Print speed	25 mm/s
Flow	1.08
Line width	0.6 mm
Wall layers	1
Infill	100%
Infill overlap	30%

settings, it is possible to achieve the best possible structure with the smallest air gaps inside the part.

The size of the nozzle must be large enough to ensure that any material containing larger particles in the solid state during printing can pass through the nozzle without the risk of clogging the nozzle. On the other hand, when increasing the nozzle size, detail accuracy of the printed part suffers. The manufacturer recommends a nozzle larger than 0.4 mm in diameter, so it was decided to use a 0.5 mm diameter nozzle. Prior to the actual printing of the heat sinks, the best possible settings for the Ice9 Rigid Nylon material were obtained by experimenting with different test pieces and adjusting the parameters based on the results until a sufficiently good result was obtained. The starting points for the parameters were obtained from the data sheet provided by the manufacturer [38]. For example, a nozzle temperature of 260 – 290 °C, a printing bed temperature of 80 – 100 °C and print speed of less than 30 mm/s are recommended.

When printing the test pieces, the material was found to be challenging to print. Adhesion between the wall layers was poor due to the rapid cooling of the material during printing. As it can be observed from the SEM image in Fig. 3, there are a lot of air gaps between the wall layers of the part. Therefore, it was decided to change the print settings for the heat sink so that the pieces were printed with only one wall layer. As a result, better contact was achieved between the internal filling structure and the outer walls of the body from a heat transfer point of view. The final printing parameters are summarised in Table 2.

3.4. Soluble support materials

The heat sinks designed using topology optimisation are challenging to manufacture even using additive manufacturing. The complex details and different cavity structures require the use of support structures to ensure successful printing. Traditionally, FFF printers use the same material for the specimen and any support structures. If the same material is used, problems arise in the removal of the support material for various cavity structures and also in the vicinity of complex details, as it may be challenging to separate the support from the actual specimen with tools.

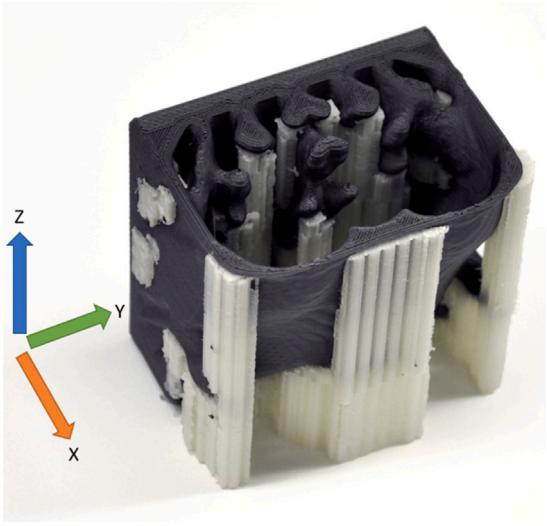

Fig. 5. Additively-manufactured topology-optimised heat sink with soluble support material. Printing direction is in the positive z-direction. Photography by Mari Rasku.

The Minifactory Ultra has two separate nozzles, where another material can be used for the support structures than for the actual part. In order to solve the issue of removing support structures, it was decided to experiment with a water-soluble support material. After printing, the water-soluble support material can simply be removed by dissolving it in water. During the study, two different support materials were tested for printing with the thermally-conductive plastic. The first material was found to adhere poorly to the thermally-conductive material, and as a result, the printed pieces failed continuously. However, the second support material, which is PVA-based, was found to work well after finding the correct printing parameters, and its adhesion and dissolution worked well for the printed topology-optimised heat sinks. Fig. 5 shows a topology-optimised heat sink with the soluble support material. It can be seen that the support material is well formed and the actual body of heat sink is of high quality despite the very challenging structure.

4. Topology optimisation process

4.1. Governing equations

The passive heat sinks are optimised using the steady-state incompressible Navier–Stokes equations coupled to the convection–diffusion equation through the Boussinesq approximation:

$$\rho_0 u_j \frac{\partial u_i}{\partial x_j} - \mu \frac{\partial}{\partial x_j}\left(\frac{\partial u_i}{\partial x_j} + \frac{\partial u_j}{\partial x_i}\right) + \frac{\partial p}{\partial x_i} + \beta_0 \rho_0 (T - T_0) g_i + \alpha(\boldsymbol{x})\, u_i = 0 \quad (2a)$$

$$\frac{\partial u_i}{\partial x_i} = 0 \quad (2b)$$

$$\rho_0 c_p u_i \frac{\partial T}{\partial x_i} - \frac{\partial}{\partial x_i}\left(k_{ij}(\boldsymbol{x}) \frac{\partial T}{\partial x_j}\right) - Q(\boldsymbol{x}) = 0 \quad (2c)$$

where u_i is the ith component of the velocity, p is the pressure, T is the temperature, ρ_0 is the fluid density at the reference temperature T_0, μ is the fluid viscosity, β_0 is the fluid volumetric thermal expansion coefficient, α is the Brinkman penalisation coefficient, c_p is the specific heat capacity, $\boldsymbol{k}$ is the thermal conductivity tensor, Q is the volumetric heat generation, and g_i is the ith component of the gravitational acceleration vector $\boldsymbol{g}$.

In order to use the governing equations for topology optimisation, the following values are spatially-varying to model a solid domain, Ω_s, immersed in a fluid domain, Ω_f. The Brinkman penalisation coefficient is defined as:

$$\alpha(\boldsymbol{x}) = \begin{cases} 0 & \text{if } \boldsymbol{x} \in \Omega_f \\ \infty & \text{if } \boldsymbol{x} \in \Omega_s \end{cases} \quad (3)$$

where an infinite value ensures that velocities are identically zero inside the solid domains. The volumetric heat generation is defined as:

$$Q(\boldsymbol{x}) = \begin{cases} Q_0 & \text{if } \boldsymbol{x} \in \omega \subset \Omega_s \\ 0 & \text{otherwise} \end{cases} \quad (4)$$

where ω is a subset of the solid domain in which a heat generation is imposed. The thermal conductivity tensor is defined as:

$$\boldsymbol{k}(\boldsymbol{x}) = \begin{cases} \boldsymbol{k}^f & \text{if } \boldsymbol{x} \in \Omega_f \\ \boldsymbol{k}^s & \text{if } \boldsymbol{x} \in \Omega_s \end{cases} \quad (5)$$

For the fluid, the thermal conductivity tensor is assumed to be isotropic:

$$\boldsymbol{k}^f = \begin{bmatrix} k^f & 0 & 0 \\ 0 & k^f & 0 \\ 0 & 0 & k^f \end{bmatrix} \quad (6)$$

For the solid layer-by-layer Ice9 Rigid Nylon material, the thermal conductivity is assumed to be isotropic within the layer (in-layer *il*) but different across the layers (cross-layer *cl*), here shown as an example for when the layers are aligned with the x–y plane:

$$\boldsymbol{k}^s = \begin{bmatrix} k^s_{il} & 0 & 0 \\ 0 & k^s_{il} & 0 \\ 0 & 0 & k^s_{cl} \end{bmatrix} \quad (7)$$

Any variations in the in-layer thermal conductivity due to filament deposition paths are neglected.

4.2. Topology optimisation formulation

In order to perform topology optimisation, the heat sink design needs to be parametrised. This is done by introducing a design field that represents the characteristic function of the solid domain:

$$\gamma(\boldsymbol{x}) = \begin{cases} 0 & \text{if } x \in \Omega_f \\ 1 & \text{if } x \in \Omega_s \end{cases} \quad (8)$$

Herein a so-called "density-based" topology optimisation approach is used, where the design field is relaxed and described using a continuous design field $\gamma(\boldsymbol{x}) \in [0;1]$ where 0 represents fully fluid, Ω_f, and 1 represents fully solid, Ω_s. Using a continuous design field allows for the use of gradient-based optimisation, which is very efficient for topology optimisation problems. However, it does introduce the possibility of intermediate design field values, which do not accurately representing either solid or fluid.

In order to represent an immersed solid geometry in a fluid domain, the two spatially-varying material properties, Eqs. (3) and (5), are coupled to the design field through interpolation functions:

$$\alpha(\boldsymbol{x}) = \alpha_{\max} \frac{1 - \gamma(\boldsymbol{x})}{1 + q_\alpha \gamma(\boldsymbol{x})} \quad (9a)$$

$$\boldsymbol{k}(\boldsymbol{x}) = \boldsymbol{k}^f + \left(\boldsymbol{k}^s - \boldsymbol{k}^f\right) \frac{\gamma(\boldsymbol{x})}{1 + q_k\,(1 - \gamma(\boldsymbol{x}))} \quad (9b)$$

where $\alpha_{\max}$ is the upper limit[1] of the Brinkman penalty coefficient, q_α is the penalisation factor for the Brinkman penalty coefficient, and q_k is the penalisation factor for the thermal conductivity. The penalisation factors are necessary to push the optimiser towards clearly defined solid–fluid designs.

4.3. Computational domain

Fig. 6 shows the computational domains for the vertical and horizontal orientations. In order to reduce computational time, symmetry is exploited: one half of the domain is simulated for the vertical orientation (Fig. 6(a)); and one quarter of the domain is simulated for the horizontal orientation (Fig. 6(b)). This explicitly enforces equivalent symmetry of the optimised design. Colours are used to indicate the different domains as follows: red = heat source; cyan = base plate; dark green = design domain; grey = insulation wall; light blue = open flow domain. The thermal energy input of 15 W is assumed evenly distributed over the heat source (red) with dimensions 56 mm × 56 mm × 15 mm yielding a volumetric heat source of 318.9 kW/m^3. A sheet of insulating material (grey) with the same conductivity as air, but impermeable, is placed around the heat source to mimic the wall and to ensure most of the heat is transferred through the heat sink. On top of the heat source, the 7 mm base plate (cyan) is enforced as solid material. On top of that, the design domain is placed according to Fig. 2. The whole heat sink setup is then embedded in a computational domain (light blue). For the vertical orientation in Fig. 6(a), the computational domain is 250 mm tall (y-direction), 200 mm wide (x-direction) and 100 mm deep (z-direction), which is then cut in half along the x-axis. For the horizontal orientation in Fig. 6(b), the computational domain is 160 mm tall (y-direction) and 200 mm wide (both x- and z-directions), which is then cut in half along the x- and z-axes.

For both orientations, the gravitational direction is set as the negative y-direction. The velocity components are set to zero inside the heat source (red) and insulation (grey) domains. The outer walls (except the top surface where $y = y_{\max}$) are all set to have a straight inflow in the normal direction with the ambient air temperature. The top surfaces are set to have a straight outflow in the normal direction. The cut surfaces have symmetry conditions imposed, which mean the normal components of the velocity and the temperature gradient are set to zero.

The ambient air temperature is set to 20 °C and the properties of air used are listed in Table 3.

[1] A non-infinite upper limit is necessary numerically. This value must be large enough to ensure insignificant velocities in the solid region, but small enough to ensure numerical stability.

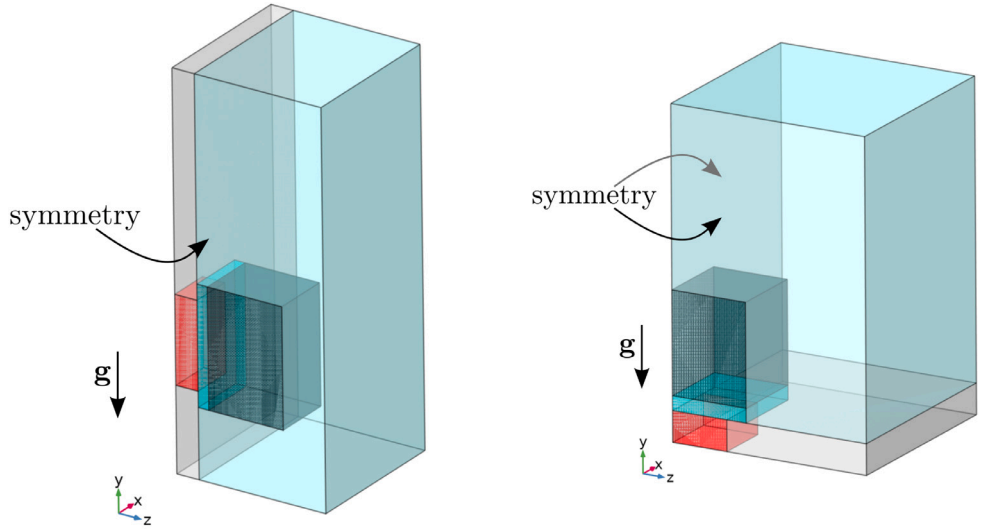

(a) Vertical orientation (b) Horizontal orientation

Fig. 6. Computational domains for the two orientations. Colours denote the following: red = heat source; cyan = base plate; dark green = design domain; grey = insulation wall; light blue = open flow domain. (For interpretation of the references to colour in this figure legend, the reader is referred to the web version of this article.)

Table 3
Material properties of air used for the topology optimisation process.

Material property	Value
Gravitational acceleration, g	9.81 m/s^2
Thermal expansion, β	3.34×10^{-3} 1/K
Kinematic viscosity, ν	1.86×10^{-5} m^2/s
Mass density, ρ	1.2 kg/m^3
Specific heat capacity, c_p	1.0×10^3 J/(kg K)
Thermal conductivity, k_f	2.6×10^{-2} W/(m K)

4.4. Optimisation details

A previously-developed large-scale parallel computing framework [34,44,45] is used to perform topology optimisation of the passive heat sinks on a high-performance computing (HPC) cluster. The topology optimisation process seeks to minimise the average temperature of the heat source under a maximum constraint on the solid material usage. The maximum volume is tuned to be approximately the same as the reference design. The conjugate heat transfer simulation uses a regular mesh of 1 mm cubic trilinear equal-order stabilised finite elements with elementwise constant design field. The Method of Moving Asymptotes (MMA) [46,47] is used to solve the optimisation problem. A reaction–diffusion filter [48] is used with a constant filter radius of 2.4 mm and a constant projection strength of 8 [49], yielding a final approximate minimum feature size of around 3 mm similar to the reference design.[2] A 4-step continuation approach is taken to gradually change certain parameters to avoid poor local minima and obtain well-defined design fields:

$$\alpha_{\max} \in \left[10^5, 10^5, 10^5, 10^6\right] \tag{10a}$$

$$q_\alpha \in [10, 10, 10, 100] \tag{10b}$$

$$q_k \in [1, 10, 100, 1000] \tag{10c}$$

[2] The imposition of minimum length scale is not exact due to the use of a projection filter, but the filter has been tuned to provide approximately the required minimum feature size.

For further information on the chosen continuation approach, the reader is referred to the previous work [34,45].

The simulations are performed on the Sophia cluster, where each node is equipped with two AMD EPYC 7351 CPUs (32 cores total) and 128 GB of RAM. For the vertical orientation (Fig. 6(a)), the computational domain is discretised using 2,520,000 elements resulting in 12,904,265 degrees-of-freedom and 72,200 design variables. The optimisation process takes approximately 18–23 h using 10 nodes (320 cores). For the horizontal orientation (Fig. 6(b)), the computational domain is discretised using 1,600,000 elements resulting in 8,211,805 degrees-of-freedom and 144,400 design variables. The optimisation process takes approximately 12–18 h using 10 nodes (320 cores).

The results from the optimisation process is a voxel-based design field, which must be converted to a surface-based geometry that can be sliced for additive manufacturing. This is done using the Paraview software [50], where an isovolume is extracted based on a threshold of $\gamma = 0.5$, then triangulated and exported to an STL file. The STL files are included as Supplementary Material to allow the reader to visually inspect the complex three-dimensional geometries.

5. Final heat sinks

A total of seven different heat sink geometries were printed for final experimental performance testing. Fig. 7 shows the reference heat sink in the thermally-conductive plastic. The build direction is from bottom to top (far to close) and each layer has the same shape. The layers are oriented to be perpendicular to the base and the heat source, such that the thermal conductivity is largest in the direction of the fins from base to tip.

Fig. 8 shows the manufactured version of the 6 different topology-optimised designs. STL files are included as Supplementary Material, making it easier for the reader to investigate the intricate designs. The first column (Figs. 8(a), 8(c) and 8(e)) are optimised for the horizontal orientation, and the second column (Figs. 8(b), 8(d) and 8(f)) are optimised for the vertical orientation. It can clearly be seen that the optimised designs for the two orientations are very different. For the horizontal case, large wall-like fins are place around the outer perimeter, with smaller pin-like fins placed in the centre. The wall-like fins have holes along the bottom to allow fresh cold air into the

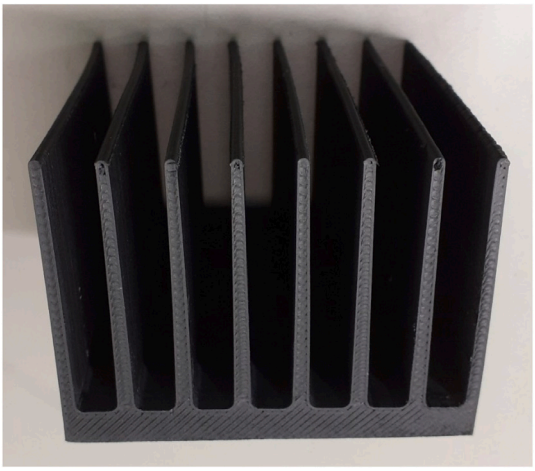

Fig. 7. Reference heat sink 3D printed with Ice9 rigid nylon without any modifications to original model.

centre of the heat sink. For the vertical case, a larger outer shell is seen, resembling the frill of a triceratops. This acts as a shroud to pull more cold air up through the heat sink to interact with the complicated pin-like fins on the inside.

For the vertical orientation, the build direction is from bottom to top in terms of height (in the positive y-direction of Fig. 6(a)). This makes it such that the cross-layer direction is in the same direction as the natural flow. This was chosen since the convective cooling will primarily be in this direction and can compensate for the low cross-layer conductivity. For the horizontal direction, the build direction is less sensitive due to the symmetry, but has to be perpendicular to the base to ensure a high in-layer thermal conductivity away from the heat source (in the x- or z-directions of Fig. 6(b)).

Figs. 8(a) and 8(b) show the printed geometries for the first topology-optimised heat sinks, designed during the iterative process of refining printing parameters and experimental and numerical setups. The thermal conductivity is assumed to be isotropic and the value is set to the in-layer value reported by the manufacturer, 4.0 W/(m K). For these results, the optimisation process did not take into account the 7 mm thick base plate described in Section 2.2. The base plate was replaced by an infinitely thin surface to which 15 W is applied.

Figs. 8(c) and 8(d) show printed geometries for the next iteration of designs, where the 7 mm base plate has been enforced during the optimisation process. The thermal conductivity is still assumed isotropic, but using the measured value of 3.23 W/(m K). It can be seen that the designs overall have the same geometries. The enforced base plate appears to have concentrated more material around the external boarders of the design domain, which makes sense since the base plate helps to distribute the heat from the heat source to the entire face of the base plate.

Figs. 8(e) and 8(f) show the printed geometries when the effective material anisotropy is taken into account by the optimisation process. The measured thermal conductivity is used, with 3.23 W/(m K) for the in-layer direction and 0.88 W/(m K) for cross-layer direction. Once again, overall the geometries are very similar to the others, but small differences are seen. For instance, a second hole has appeared in the shroud for the vertical design in Fig. 8(f).

6. Experimental testing

For testing the heat sinks, an experimental setup was constructed to test the performance. Based on the results, the thermal resistance of the heat sinks are calculated and used to compare their performance.

6.1. Equipment and setup

The heat sinks are attached to the heat source and the wall structure as shown in Fig. 10. In addition to the elements shown, a 150 mm thick polyurethane insulating plate (FinnFoam FF-PIR 150) was attached to the back of the heat source. The insulating plate was 400 mm × 400 mm and the thermal conductivity was 0.022 W/(m K). This is to prevent heat transfer to the environment from the back of the heat source. Due to the large size of the insulation plate and its poor thermal conductivity, the insulation was assumed to be perfect and all thermal energy to pass through the heat sink to be tested. In the experimental setup, the heat source consists of power resistors mounted on an aluminium plate and an additively-manufactured insulating housing solution. The heat equalising aluminium plate was 56 mm × 56 mm in size, corresponding to the heat source specified in Fig. 2. The resistors are controlled by a laboratory power supply and their power is determined by measuring current and voltage separately with multimeters. A 200 µm thick heat conductive graphite sheet is placed between the heat sink to be tested and the heat source, to ensure good thermal contact between them. The surface of the heat sink to be tested are sanded smooth with fine sandpaper after printing to smooth out slightly uneven surfaces. The heat source is attached to the heat sink and the wall structure with four screws. To ensure consistent thermal contact, each of the four screws were tightened to the same torque of 0.42 N m using an electric screwdriver and the thermal interface material was replaced each time a new heat sink was tested.

A K-type temperature sensor was mounted at the base of the heat sink to measure the base temperature, T_b, as shown in Fig. 9. The sensor was installed through a hole in the aluminium plate and was trapped between the housing structure of the heat source and the bottom plate of the heat sink with a flexible pad. There was a hole in the thermal interface material for the sensor, so the sensor was in direct contact with the heat sink. The ambient temperature was monitored by a second temperature sensor. The experimental setup also included a thermal camera and a computer to operate thermal camera and save images.

The heat sinks are tested in two different installation directions, as the starting point of the study is to design topology-optimised structures for the cases of the two different installation directions. The test situation in the case of the vertical mounting direction is shown in Fig. 10. For testing the horizontal mounting direction, the wall structure shown in Fig. 10 is turned parallel to the table plane, supported by aluminium profiles so that the insulating plate could also be fitted to the back of the heat source in this situation. The reference heat sinks, i.e. the extruded aluminium and additively-manufactured plastic straight-fin heat sinks, are also tested in both installation directions in order to provide data to compare the topology-optimised designs with in both cases.

6.2. Heat sink testing

The power of the heat source is kept at 15 W by adjusting the voltage of the laboratory power supply based on the measured voltage and current values. During the measurement, the base temperature of the heat sink T_b and the ambient temperature T_a are monitored. The measurements are continued until an equilibrium is reached, where the temperature difference $T_b - T_a$ no longer changes. The measured values of the electric current, supplied voltage, and the temperature values of the sensors, are recorded in the measurement report. Thermal camera images are also recorded from the situation for later review. Fig. 11 is a thermal camera image of the *Vert_Iso_Rep* heat sink during testing. The figure shows the heat sink surface temperature and the effect of the natural convective plume on the back wall.

6.3. Test results

After testing the heat sinks, the thermal resistance of each heat sink is calculated based on the measured values. The calculation of the

(a) Horizontal, isotropic, reported - *Horiz_Iso_Rep*

(b) Vertical, isotropic, reported - *Vert_Iso_Rep*

(c) Horizontal, isotropic, measured - *Horiz_Iso_Meas*

(d) Vertical, isotropic, measured - *Vert_Iso_Meas*

(e) Horizontal, anisotropic, measured - *Horiz_Aniso_Meas*

(f) Vertical, anisotropic, measured - *Vert_Aniso_Meas*

Fig. 8. Topology-optimised heat sinks optimised under various assumptions: (a,b) isotropic thermal conductivity using the in-layer value reported by the manufacturer [38] and without a specified base plate; (c,d) isotropic thermal conductivity using the in-layer measured value (Table 1) and with a specified base plate; (e,f) anisotropic thermal conductivity using the measured values (Table 1) and with a specified base plate. The naming scheme defines first the orientation, then material behaviour, then source of values. STL files are included as Supplementary Material. Photography by Mari Rasku.

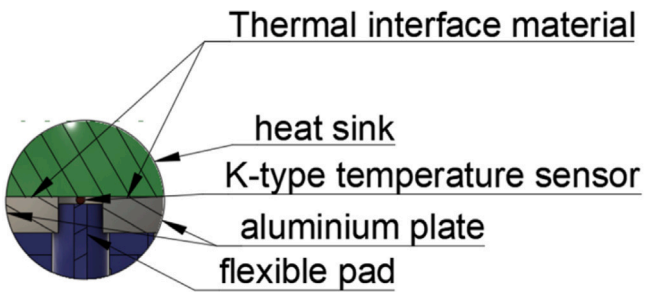

Fig. 9. Detailed cross-sectional view of the installation of a K-type temperature sensor to measure the base temperature of the heat sink.

thermal resistance is carried out according to:

$$R_{\text{th}} = \frac{\Delta T}{Q} = \frac{T_b - T_a}{U \cdot I} \tag{11}$$

where T_b is the base temperature of the heat sink, T_a is the ambient temperature, U is voltage of the heat source and I is current of the heat source. The values in the measurement report used to calculate the thermal resistances are given in Appendix A. The calculation of the measurement error for thermal resistance is carried out using partial derivatives:

$$\Delta R_{\text{th}} \leq \left|\frac{\partial R_{\text{th}}}{\partial T_b}\Delta T_b\right| + \left|\frac{\partial R_{\text{th}}}{\partial T_a}\Delta T_a\right| + \left|\frac{\partial R_{\text{th}}}{\partial U}\Delta U\right| + \left|\frac{\partial R_{\text{th}}}{\partial I}\Delta I\right| \tag{12}$$

where ΔT_b is the measurement error of base temperature of the heat sink, ΔT_a is the measurement error of ambient temperature, ΔU is

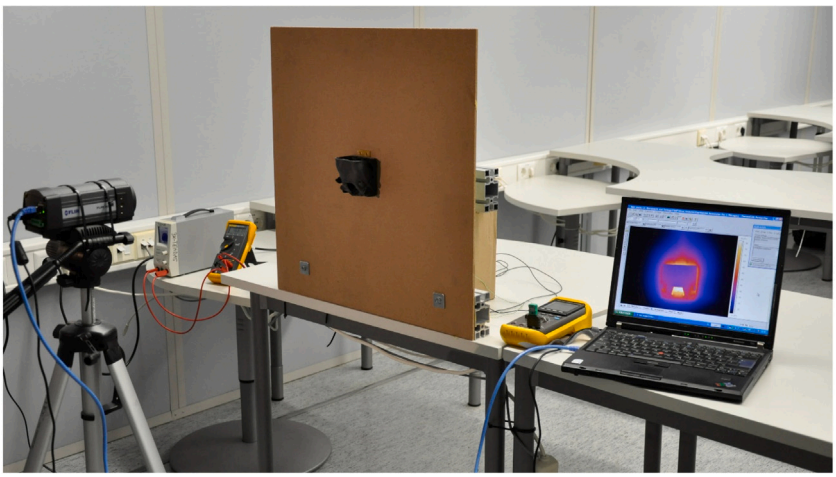

Fig. 10. Test arrangement for vertical installation direction. Heat sink to be tested was attached to heat source and wall structure. The horizontal mounting direction was measured with the same equipment by turning the plate horizontally.

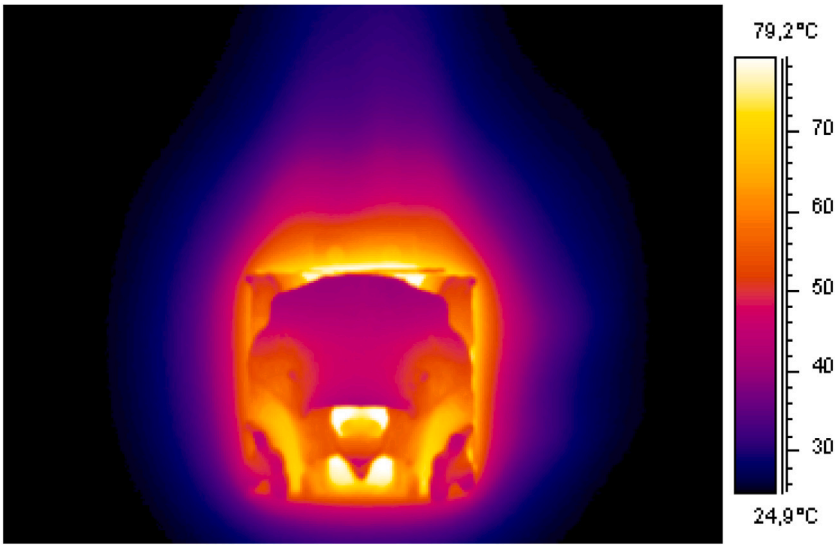

Fig. 11. Thermal camera image of the *Vert_Iso_Rep* heat sink.

Table 4
Heat sink thermal resistance, improvement in percent, volume and surface area for the vertical mounting direction at $Q = 15$ W.

Heat sink	Resistance [K/W]	Improvement [%]	Volume [cm^3]	Surface area [cm^2]
Reference - aluminium	1.84 ± 0.05	–	118.6	690.8
Reference - Ice9	4.56 ± 0.05	–	118.6	690.8
Vert_Iso_Rep	4.32 ± 0.05	5.3	128.1	359.0
Vert_Iso_Meas	4.17 ± 0.05	8.6	109.3	346.5
Vert_Aniso_Meas	4.10 ± 0.05	10.1	109.1	359.3

Table 5
Heat sink thermal resistance, improvement in percent, volume and surface area for the horizontal mounting direction at $Q = 15$ W.

Heat sink	Resistance [K/W]	Improvement [%]	Volume [cm^3]	Surface area [cm^2]
Reference - aluminium	1.91 ± 0.05	–	118.6	690.8
Reference - Ice9	4.88 ± 0.06	–	118.6	690.8
Horiz_Iso_Rep	4.13 ± 0.05	15.4	128.0	394.6
Horiz_Iso_Meas	3.90 ± 0.05	20.1	108.8	409.6
Horiz_Aniso_Meas	3.95 ± 0.05	19.7	108.5	395.8

measurement error of voltage of the heat source and ΔI is measurement error of current of the heat source.

The calculated thermal resistances are shown in Table 4 for the vertical mounting direction and Table 5 for the horizontal mounting direction. The tables also present the thermal resistance improvement of each optimised heat sink compared to the reference plastic heat sink test result, as well as the volume and surface area of each design computed from the STL files used for manufacture.

From Table 4, it can be seen that topology-optimised heat sinks achieve a 5 – 10% improvement compared to the reference design in the vertical mounting direction. The order of performance for the heat sinks meets expectations. The first model, *Vert_Iso_Rep*, in which the

base plate is not taken into account, offers a 5.3% improvement. The improvement increases to 8.6% for the second model, *Vert_Iso_Meas*, where the base plate is taken into account and the measured in-layer thermal conductivity is used. This makes sense since the optimisation is based on a better representation of the experimental setup. The best performance of all is provided by the last design, *Vert_Aniso_Meas*, which is optimised based on the anisotropic nature of the thermal conductivity due to the manufacturing technology. A better representation of the physical system again leads to better performance.

For the horizontal mounting direction, Table 5 shows that topology-optimised heat sinks achieve a $15-20\%$ improvement compared to the reference design. The order of performance is not quite as expected. The second model, *Horiz_Iso_Meas*, uses a more accurate model and therefore the optimised design performs better than the first model, *Horiz_Iso_Rep*. However, the design optimised taking the anisotropic thermal conductivity into account, *Horiz_Aniso_Meas*, performs slightly worse that the one that assumes an isotropic conductivity, *Horiz_Iso_Meas*. As will be discussed in Section 7, the most likely cause of this anomaly is deformation of the heat sink base observed during the measurement.

The observed performance improvements should be seen in the light of the substantially lower surface area exhibited by all topology-optimised designs and a comparable material volume, as listed in Tables 4 and 5. The initial designs, *Vert_Iso_Rep* and *Horiz_Iso_Rep*, were optimised with a larger maximum volume constraint which was not yet tuned to the final reference design, and thus their final volume is slightly larger than the reference. The subsequent designs were optimised using a maximum volume constraint tuned to the reference design, but the final design volumes are slightly lower due to numerical reasons.[3] The surface areas are seen to be as far as $41-48\%$ lower than the reference heat sink, yet they perform $5-20\%$ better in terms of thermal resistance. This clearly shows that cooling performance of passive heat sinks are not merely driven by maximisation of surface area. The correct placement of the surface area and the conducting geometry is significantly more important. This is perfectly in line with previous observations [25,34].

7. Discussion

Significant effort has been put into ensuring that the effect of the printing process, in the comparison of the heat sinks, has been kept to a minimum. The print settings were tuned using initial tests and other geometries, to ensure the best possible printing of the heat sinks. Subsequently the same settings and a consistently controlled printing environment was used. However, the print setting may not be optimal in terms of cooling properties. This could be further improved based on a suitable thermal conductivity test as a basis for further research.

Based on the experimental measurements, topology-optimised heat sinks achieve a 5–10% improvement in the thermal resistance for the vertical installation direction and a 15–20% improvement for the horizontal direction. The performance improvement is less in the vertical installation direction, mainly because the reference straight-fin performs very well with the fins oriented in the direction of gravity.

During testing, the base plate of the *Horiz_Aniso_Meas* heat sink was observed to significantly distort as shown in Fig. 12. The base plate appeared planar after manufacture and before testing began. As a result of the distortion, an air gap was formed between the contact surface of the heat source and the heat sink despite the conductive graphite sheet installed between the surfaces. It is clear that this had a degrading effect on its cooling properties, clearly observed in a slightly higher thermal resistance than expected. That heat sink was reprinted to determine whether the phenomenon was a random occurrence. The reprinted model experienced exactly the same phenomenon. Based on this and the fact that it was not observed for any of the other prints, it is believe that the large distortion must be due to the structure of the heat sink, rather than an error in the printing process. Thermal stresses during heating of the heat sink could be causing the heat sink to bend and lose contact. Further investigation into the cause of this phenomenon is left as future research. Once the phenomenon is understood, the distortion of the heat sink could potentially be minimised by taking into account the thermal stresses in the topology optimisation process in the future.

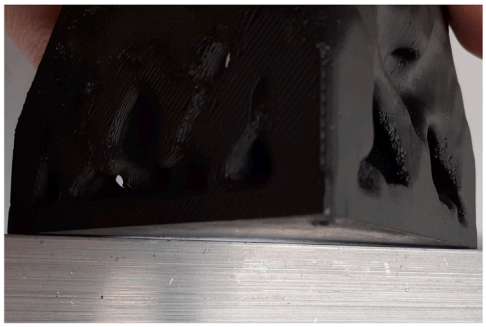

Fig. 12. Base plate of the *Horiz_Aniso_Meas* heat sink. Distortion of the bottom flat surface is noticeable when compared to a straight metal plate.

The performance of the thermally-conductive Ice9 Rigid Nylon filament can be compared to aluminium, which is commonly used in heat sinks, by comparing the thermal resistance of the reference heat sinks made of both materials. Based on the measurements in the vertical direction, the thermal resistances were determined to be 1.84 K/W and 4.56 K/W. This means in theory that the aluminium heat sink is capable of transferring 148% more thermal power at the same temperature. In the horizontal direction, the corresponding thermal resistance values are 1.91 K/W and 4.88 K/W, yielding an improvement of 155%. It should be noted that the performance of materials cannot be directly compared by thermal conductivity or even on the basis of the measurements made on individual geometries. The difference between the materials depends entirely on the application and the geometry of the heat sink.

8. Conclusions

It can be concluded that topology optimisation can achieve improved performance of passive heat sinks produced using material extrusion of a thermally-conductive plastic filament. The best designs obtain a 10% and 20% lower thermal resistance compared to the reference straight-fin heat sink in the vertical and horizontal installation direction, respectively. This is achieved using measured thermal conductivity values under isotropic and anisotropic assumptions. For the vertical direction, the best performance is obtained with an anisotropic thermal conductivity model. However, for the horizontal direction, the design optimised using anisotropic properties exhibited significant distortion of the base plate. The distortion causes an air gap between the heat sink base plate and the heat source, which impairs heat transfer.

It can also be concluded that topology-optimised passive heat sinks can be additively manufactured using a fully controlled material extrusion printing environment. The chosen printing parameters gives good results, but can potentially be improved further with specifically thermal performance in mind.

[3] Due to the filtering procedure that is used to impose a minimum feature size, an intermediate region around the solid–fluid interface is present and causes minor deviations of the final volume for surface extracted designs.

Table A.6
Measurement report for the measurements used in this paper.

Specimen	Voltage U [V]	Current I [A]	Power Q [W]	Base temp. T_b [°C]	Ambient temp. T_a [°C]	Temp. diff. ΔT [°C]
Reference aluminium (vertical)	16.61	0.918	15.25	48.5	20.5	28.0
Reference aluminium (horizontal)	16.61	0.918	15.25	49.6	20.5	29.1
Reference plastic (vertical)	16.41	0.919	15.08	93.8	25.0	68.8
Reference plastic (horizontal)	16.37	0.912	14.93	98.4	25.5	72.9
Vert_Iso_Rep	16.59	0.918	15.23	87.0	21.2	65.8
Horiz_Iso_Rep	16.63	0.915	15.22	85.6	22.8	62.8
Vert_Iso_Meas	16.61	0.912	15.15	83.5	20.4	63.1
Horiz_Iso_Meas	16.63	0.912	15.17	79.9	20.8	59.1
Vert_Aniso_Meas	16.60	0.916	15.21	83.1	20.7	62.4
Horiz_Aniso_Meas	16.62	0.917	15.21	83.4	23.4	60.0

CRediT authorship contribution statement

Eetu Huttunen: Writing – review & editing, Writing – original draft, Methodology, Investigation, Data curation, Conceptualization. **Mikko T. Nykänen:** Writing – review & editing, Writing – original draft, Supervision, Resources, Project administration, Methodology, Investigation. **Joe Alexandersen:** Writing – review & editing, Writing – original draft, Supervision, Software, Resources, Methodology, Investigation.

Declaration of competing interest

The authors declare that they have no known competing financial interests or personal relationships that could have appeared to influence the work reported in this paper.

Data availability

The optimised geometries have been made freely available as STL files. All experimental data is available upon request. The numerical code is not available, but help will be provided if necessary.

Acknowledgements

The authors wish to thank Mari Rasku for the photographs of the manufactured specimens and XAMK Mikpolis materials technology laboratory for SEM images. The computations were performed on the Sophia cluster through the Danish e-Infrastructure Cooperation (Project ID DEIC-SDU-L-5). Lastly, the authors wish to thank the Electronics 3K Factory at XAMK for providing the heat sink manufacturing and testing equipment. The heat sinks were printed in an additive manufacturing piloting environment at Electronics 3K Factory. Likewise, all material testing and heat sink performance testing were performed at the Electronics 3K Factory.

Appendix A. Measurement report

Table A.6 shows the measurement report for the experimental values used in this paper. Furthermore, the following is an example of error calculation for "Reference aluminium (horizontal)":

$$\Delta R_{\text{th}} \leq |0.07 \times 0.35| + |-0.07 \times 0.35| + |-0.1 \times 0.0002| + |-2.0 \times 0.0012| \leq 0.048 \approx 0.05 \quad \text{(A.1)}$$

Appendix B. Supplementary data

Supplementary material related to this article can be found online at https://doi.org/10.1016/j.addma.2022.103123. The supplementary material consists of STL geometry files for the optimised geometries shown in the manuscript.

References

[1] C.-H. Ahn, J. Oh, Resistive grounding technique of heat sink for reducing radiation noise, J. Electr. Eng. Technol. 9 (5) (2014) 1724–1728.
[2] R. Whitt, S. Hudson, D. Huitink, Z. Yuan, A. Emon, F. Luo, Additive manufactured impinging coolant, low electromagnetic interference, and nonmetallic heat spreader: Design and optimization, J. Electron. Packag. 142 (4) (2020) http://dx.doi.org/10.1115/1.4048493, 041004.
[3] B.M. Nafis, R. Whitt, A.-C. Iradukunda, D. Huitink, Additive manufacturing for enhancing thermal dissipation in heat sink implementation: A review, Heat Transf. Eng. 42 (12) (2021) 967–984, http://dx.doi.org/10.1080/01457632.2020.1766246.
[4] I. Kaur, P. Singh, State-of-the-art in heat exchanger additive manufacturing, Int. J. Heat Mass Transfer 178 (2021) 121600, http://dx.doi.org/10.1016/j.ijheatmasstransfer.2021.121600.
[5] C. Zhang, Y. Li, W. Kang, X. Liu, Q. Wang, Current advances and future perspectives of additive manufacturing for functional polymeric materials and devices, SusMat 1 (1) (2021) 127–147, http://dx.doi.org/10.1002/sus2.11.
[6] M.P. Bendsøe, O. Sigmund, Topology Optimization: Theory, Methods, and Applications, second ed., Springer-Verlag Berlin Heidelberg, 2004, http://dx.doi.org/10.1007/978-3-662-05086-6.
[7] N. Nguyen, J.G. Park, S. Zhang, R. Liang, Recent advances on 3D printing technique for thermal-related applications, Adv. Energy Mater. 20 (5) (2018) 1700876, http://dx.doi.org/10.1002/adem.201700876.
[8] H. Prajapati, D. Ravoori, R.L. Woods, A. Jain, Measurement of anisotropic thermal conductivity and inter-layer thermal contact resistance in polymer fused deposition modeling (FDM), Addit. Manuf. 21 (2018) 84–90, http://dx.doi.org/10.1016/j.addma.2018.02.019.
[9] J. Jing, Y. Chen, S. Shi, L. Yang, P. Lambin, Facile and scalable fabrication of highly thermal conductive polyethylene/graphene nanocomposites by combining solid-state shear milling and FDM 3D-printing aligning methods, Chem. Eng. J. 402 (2020) 126218, http://dx.doi.org/10.1016/j.cej.2020.126218.
[10] H. Guo, H. Zhao, H. Niu, Y. Ren, H. Fang, X. Fang, R. Lv, M. Maqbool, S. Bai, Highly thermally conductive 3D printed graphene filled polymer composites for scalable thermal management applications, ACS Nano 15 (4) (2021) 6917–6928, http://dx.doi.org/10.1021/acsnano.0c10768.
[11] K. Timbs, M. Khatamifar, E. Antunes, W. Lin, Experimental study on the heat dissipation performance of straight and oblique fin heat sinks made of thermal conductive composite polymers, Therm. Sci. Eng. Prog. 22 (2021) 100848, http://dx.doi.org/10.1016/j.tsep.2021.100848.
[12] J.K. Liu, A.T. Gaynor, S.K. Chen, Z. Kang, K. Suresh, A. Takezawa, L. Li, J. Kato, J.Y. Tang, C.C.L. Wang, L. Cheng, X. Liang, A.C. To, Current and future trends in topology optimization for additive manufacturing, Struct. Multidiscip. Optim. 57 (6) (2018) 2457–2483, http://dx.doi.org/10.1007/s00158-018-1994-3.
[13] P. Zhang, J.K. Liu, A.C. To, Role of anisotropic properties on topology optimization of additive manufactured load bearing structures, Scr. Mater. 135 (2017) 148–152, http://dx.doi.org/10.1016/j.scriptamat.2016.10.021.
[14] A.M. Mirzendehdel, B. Rankouhi, K. Suresh, Strength-based topology optimization for anisotropic parts, Addit. Manuf. 19 (2018) 104–113, http://dx.doi.org/10.1016/j.addma.2017.11.007.
[15] C. Dapogny, R. Estevez, A. Faure, G. Michailidis, Shape and topology optimization considering anisotropic features induced by additive manufacturing processes, Comput. Methods Appl. Mech. Engrg. 344 (2019) 626–665, http://dx.doi.org/10.1016/j.cma.2018.09.036.
[16] J.P. Zhang, S.S. Wang, G.Q. Zhou, S.G. Gong, S.H. Yin, Topology optimization of thermal structure for isotropic and anisotropic materials using the element-free Galerkin method, Eng. Optim. 52 (7) (2020) 1097–1118, http://dx.doi.org/10.1080/0305215x.2019.1636979.
[17] D.R. Jantos, K. Hackl, P. Junker, Topology optimization with anisotropic materials, including a filter to smooth fiber pathways, Struct. Multidiscip. Optim. 61 (5) (2020) 2135–2154, http://dx.doi.org/10.1007/s00158-019-02461-x.
[18] E.M. Dede, T. Nomura, J. Lee, Thermal-composite design optimization for heat flux shielding, focusing, and reversal, Struct. Multidiscip. Optim. 49 (1) (2014) 59–68, http://dx.doi.org/10.1007/s00158-013-0963-0.

[19] J. Alexandersen, C.S. Andreasen, A review of topology optimisation for fluid-based problems, Fluids 5 (1) (2020) http://dx.doi.org/10.3390/fluids5010029.
[20] A.A. Koga, E.C.C. Lopes, H.F. Villa Nova, C.R.d. Lima, E.C.N. Silva, Development of heat sink device by using topology optimization, Int. J. Heat Mass Transfer 64 (2013) 759–772, http://dx.doi.org/10.1016/j.ijheatmasstransfer.2013.05.007.
[21] S. Zeng, B. Kanargi, P.S. Lee, Experimental and numerical investigation of a mini channel forced air heat sink designed by topology optimization, Int. J. Heat Mass Transfer 121 (2018) 663–679, http://dx.doi.org/10.1016/j.ijheatmasstransfer.2018.01.039.
[22] S. Zeng, P.S. Lee, Topology optimization of liquid-cooled microchannel heat sinks: An experimental and numerical study, Int. J. Heat Mass Transfer 142 (2019) http://dx.doi.org/10.1016/j.ijheatmasstransfer.2019.07.051.
[23] E.M. Dede, S.N. Joshi, F. Zhou, Topology optimization, additive layer manufacturing, and experimental testing of an air-cooled heat sink, J. Mech. Des. 137 (11) (2015) 111403–111403–9, http://dx.doi.org/10.1115/1.4030989.
[24] S. Jahan, T. Wu, Y. Shin, A. Tovar, H. El-Mounayri, Thermo-fluid topology optimization and experimental study of conformal cooling channels for 3D printed plastic injection molds, Procedia Manuf. 34 (2019) 631–639, http://dx.doi.org/10.1016/j.promfg.2019.06.120.
[25] B.S. Lazarov, O. Sigmund, K.E. Meyer, J. Alexandersen, Experimental validation of additively manufactured optimized shapes for passive cooling, Appl. Energy 226 (2018) 330–339, http://dx.doi.org/10.1016/j.apenergy.2018.05.106.
[26] T. Lei, J. Alexandersen, B.S. Lazarov, F. Wang, J.H.K. Haertel, S. De Angelis, S. Sanna, O. Sigmund, K. Engelbrecht, Investment casting and experimental testing of heat sinks designed by topology optimization, Int. J. Heat Mass Transfer 127 (2018) 396–412, http://dx.doi.org/10.1016/j.ijheatmasstransfer.2018.07.060.
[27] T. Zhou, B. Chen, H. Liu, Study of the performance of a novel radiator with three inlets and one outlet based on topology optimization, Micromachines 12 (6) (2021) http://dx.doi.org/10.3390/mi12060594.
[28] S. Qian, S. Lou, C. Ge, W. Wang, X. Tian, Y. Cai, The influence of temperature dependent fluid properties on topology optimization of conjugate heat transfer, Int. J. Therm. Sci. 173 (2022) 107424, http://dx.doi.org/10.1016/j.ijthermalsci.2021.107424.
[29] X. Li, L. Zhang, B. Li, Heat transfer augmentation in microchannel heat sink based on isogeometric topology optimization framework, Appl. Math. Model. 104 (2022) 163–187, http://dx.doi.org/10.1016/j.apm.2021.11.021.
[30] X.-h. Han, H.-l. Liu, G. Xie, L. Sang, J. Zhou, Topology optimization for spider web heat sinks for electronic cooling, Appl. Therm. Eng. 195 (2021) 117154, http://dx.doi.org/10.1016/j.applthermaleng.2021.117154.
[31] J.S. Lee, S.Y. Yoon, B. Kim, H. Lee, M.Y. Ha, J.K. Min, A topology optimization based design of a liquid-cooled heat sink with cylindrical pin fins having varying pitch, Int. J. Heat Mass Transfer 172 (2021) 121172, http://dx.doi.org/10.1016/j.ijheatmasstransfer.2021.121172.
[32] F. Incropera, D. Dewitt, T. Bergman, A. Lavine, Principles of Heat and Mass Transfer, eighth ed., Wiley, 2017.
[33] A. Bar-Cohen, W.M. Rohsenow, Thermally optimum spacing of vertical, natural convection cooled, parallel plates, J. Heat Transfer 106 (1) (1984) 116–123, http://dx.doi.org/10.1115/1.3246622.
[34] J. Alexandersen, O. Sigmund, K.E. Meyer, B.S. Lazarov, Design of passive coolers for light-emitting diode lamps using topology optimisation, Int. J. Heat Mass Transfer 122 (2018) 138–149, http://dx.doi.org/10.1016/j.ijheatmasstransfer.2018.01.103.
[35] ASTM, ISO/ASTM 52900:2015, Additive manufacturing - General principles - Terminology, Standard, 2015.
[36] A. Thermalloy, Data sheet (637303b03000), 2021, Web document, accessed 8/12-2021. URL: https://docs.rs-online.com/ce20/0900766b80978dea.pdf.
[37] TCPoly, Safety data sheet (Ice9 rigid), 2020, Web document, accessed on 8/12-2021. URL: https://tcpoly.com/wp-content/uploads/2020/08/SDS_Ice9_Rigid_R02.pdf.
[38] TCPoly, Technical data sheet (Ice9 rigid), 2019, Web document, accessed 8/12-2021. URL: https://tcpoly.com/wp-content/uploads/2021/08/ice9_Rigid_r405.pdf.
[39] I.-L. Ngo, S. Jeon, C. Byon, Thermal conductivity of transparent and flexible polymers containing fillers: A literature review, Int. J. Heat Mass Transfer 98 (2016) 219–226, http://dx.doi.org/10.1016/j.ijheatmasstransfer.2016.02.082.
[40] ASTM International, ASTM C1044-98, Standard Practice for Using a Guarded-Hot-Plate Apparatus or Thin-Heater Apparatus in the Single-Sided Mode, Standard, 2003.
[41] ASTM, ASTM C177-97, Standard Test Method For Steady-State Heat Flux Measurements And Thermal Transmission Properties by Means of the Guarded-Hot-Plate Apparatus, Standard, 1997.
[42] miniFactory, Data sheet (Ultra 3D), 2021, Web document, accessed 8/12-2021. URL: https://minifactory.fi/wp-content/uploads/2021/11/miniFactory-Ultra-2021-1.pdf.
[43] miniFactory, Materials & applications, 2021, Web document, accessed 8/12-2021. URL: https://minifactory.fi/wp-content/uploads/2021/11/miniFactory-Materials-2021-1.pdf.
[44] N. Aage, E. Andreassen, B.S. Lazarov, Topology optimization using PETSc: An easy-to-use, fully parallel, open source topology optimization framework, Struct. Multidiscip. Optim. 51 (3) (2015) 565–572, http://dx.doi.org/10.1007/s00158-014-1157-0.
[45] J. Alexandersen, O. Sigmund, N. Aage, Large scale three-dimensional topology optimisation of heat sinks cooled by natural convection, Int. J. Heat Mass Transfer 100 (2016) 876–891, http://dx.doi.org/10.1016/j.ijheatmasstransfer.2016.05.013.
[46] K. Svanberg, The method of moving asymptotes—a new method for structural optimization, Internat. J. Numer. Methods Engrg. 24 (2) (1987) 359–373, http://dx.doi.org/10.1002/nme.1620240207.
[47] N. Aage, B.S. Lazarov, Parallel framework for topology optimization using the method of moving asymptotes, Struct. Multidiscip. Optim. 47 (4) (2013) 493–505, http://dx.doi.org/10.1007/s00158-012-0869-2.
[48] B.S. Lazarov, O. Sigmund, Filters in topology optimization based on Helmholtz-type differential equations, Internat. J. Numer. Methods Engrg. 86 (6) (2011) 765–781, http://dx.doi.org/10.1002/nme.3072.
[49] B.S. Lazarov, F. Wang, O. Sigmund, Length scale and manufacturability in density-based topology optimization, Arch. Appl. Mech. 86 (1–2) (2016) 189–218, http://dx.doi.org/10.1007/s00419-015-1106-4.
[50] J.P. Ahrens, B. Geveci, C.C. Law, ParaView: An end-user tool for large-data visualization, in: The Visualization Handbook, 2005.